Journal of Applied Fluid Mechanics, Vol. 18, No. 9, pp. 2406-2420, 2025.
Available online at www.jafmonline.net, ISSN 1735-3572, EISSN 1735-3645.
https://doi.org/10.47176/jafm.18.9.3357

Heat Dissipation Performance Analysis of Semiconductor Lasers with Microchannel Structure Inspired by Biomimetic Plant Leaves

Z. Hou[1], Z. Zhou[1], K. Zhang[1], Y. Ji[1], Y. Zheng[1], L. Wang[2†] and S. Li[3]

[1]*School of Mechanical and Vehicular Engineering, Changchun University, Changchun 130022, China*
[2] *Jilin Science and Technology Innovation Center of Green Synthesis and New Materials Research and Development, Jilin Engineering Normal University, Changchun, Jilin 130052, China*
[3]*Changchun New Industries Optoelectronics Technology Co., Ltd. Lasers, Optics & Photonics, Jilin 130012, China*

†*Corresponding Author Email: wanglb733@nenu.edu.cn*

ABSTRACT

Semiconductor lasers generate a significant amount of heat during operation, which can lead to various issues, including performance degradation and structural deformation of the housing. To address these challenges, this study proposes a novel cooling channel design inspired by the natural vascular architecture of plant leaves. This biomimetic design, referred to as the bionic vane cooling channel, has been optimized by manipulating key variables such as the height of the cooling gap, the angle between the primary and secondary channels, and the rate of water flow at the inlet. A comprehensive series of computational fluid dynamics (CFD) simulations and numerical analyses were conducted. The results indicate that with a constant inlet Reynolds number (Re), an increase in the height of the cooling gap significantly enhances the heat dissipation capacity. Specifically, when the cooling gap height in type I, type II, and type III structures is increased from 2 mm to 4 mm, the Nusselt Number (Nu) improves by 25.74%, 12.48%, and 15.80%, respectively. Additionally, adjusting the angle between the primary and secondary channels also increases the heat dissipation capacity. For example, increasing the angle from 45° to 65° results in Nu improvements of 42.07%, 26.07%, and 30.84% for Models I, II, and III, respectively. At a Reynolds number of 20,000, the enhancements in Nu were found to be 90.96%, 36.19%, and 50.41%, respectively. The study further includes a simulation analysis of the radiator's structural deformation. The findings suggest that increasing the angle between the primary and secondary channels can significantly reduce deformation. For instance, at an angle of 45°, deformation exceeded 4 × 10-3 mm, whereas at 65°, the deformation was less than 1 × 10-3 mm. This study introduces a novel approach to enhancing both the heat dissipation efficiency and the operational stability of semiconductor lasers.

Article History

Received January 5, 2025
Revised April 11, 2025
Accepted April 13, 2025
Available online July 5, 2025

Keywords:

Semiconductor lasers
Microchannel
Radiator
Computational fluid dynamics
Heat dissipation
Biomimetic plant leaves

1. INTRODUCTION

Semiconductor lasers are utilized extensively across various fields such as industry, medicine, aerospace, radar, measurement, and detection. Currently, semiconductor lasers face numerous challenges, particularly in terms of efficiency and thermal management. The electro-optical conversion efficiency of these lasers is approximately 70%, which leads to significant heat generation during operation. This heat increases the temperature of the semiconductor laser chip, causing issues such as a shift in the center wavelength, broadening of the spectral width, reduction in output power, and decreased reliability.

In response to these challenges, extensive research has been conducted globally. Ma C and colleagues designed a fluid guiding layer that not only provides efficient fluid distribution and lower pressure drops but also supports the trend towards the miniaturization of electronic systems while significantly reducing the energy consumption needed for heat dissipation (Ma et al., 2023). Song and their team demonstrated through modeling and simulation that heat exchangers with slots offer superior heat transfer performance compared to those without slots (Song et al., 2020). Zheng and associates found that hierarchical radiators exhibit better heat transfer performance than traditional radiators (Zheng et al., 2020). Xiang developed microchannel radiators that outperform conventional metal solid radiators in terms of heat dissipation (Xiang et al.,

Nomenclature

Nu	Nusselt Number	T_f	average temperature of the shell
Re	Reynolds number	T_w	average temperature of the working medium
H	height of heat sink gap	q_{max}	maximum thermal efficiency
ρ	fluid density	Q	total amount of heat dissipation
μ	fluid viscosity	A	heat dissipation area
λ	thermal conductivity	V_{outmax}	maximum exit speed
ρF	body force per unit volume	V_{outave}	average speed of exports
S_h	heat source within the fluid,	T_{ave}	overall average temperature
$divP$	divergence of the stress tensor per unit volume	Δx	overall average deformation
Φ	dissipation function	type I	β=45°
θ	temperature uniformity index	type II	β=55°
T_{max}	maximum shell temperature	type III	β=65°
T_{min}	minimum shell temperature	Model I	H=2 mm
$\bar{v}$	average speed	Model II	H=3 mm
d	length Characteristics	Model III	H=4 mm
h_1	specific enthalpy of the fluid	Kind I	H=2 mm, β=65°
h_2	convective heat transfer coefficient of the working medium	Kind II	H=3 mm, β=55°
k	thermal conductivity of the working medium	Kind III	H=4mm, β=65°
β	angle between two channels		

2022). Li introduced microchannel radiators simulating MCTVs and designed three new microchannels with PECs greater than those of straight microchannels (Sun et al., 2020). Zhao explored the forced convection heat transfer characteristics of microchannel radiators through numerical analysis and also investigated the impact of different boundary conditions on overall heat transfer (Zhao et al., 2002). Zhao investigated the effect of heat flow on the thermal performance of MCOHPs and discovered that using graphene nanofluid as a working medium could reduce thermal resistance by 83.6% and increase the maximum thermal conductivity by 105% (Zhao et al., 2023). Li demonstrated that the Nusselt number (Nu) of the nanofluid was 1.12-1.66 times higher than that of deionized water, confirming significant heat transfer enhancement in Al_2O_3-water nanofluids (Li et al., 2020). Tan enhanced the heat transfer performance of a system by doping Al_2O_3 nanoparticles into the working medium. Compared to pure water, the heat transfer power of the system using Al_2O_3 nanofluid at a mass fraction of 0.7% was significantly increased by 11.17%, and the energy consumption ratio was enhanced by 6.40% (Tan et al., 2024). Lastly, Li demonstrated the effectiveness of chalcogenide nanoplate lasers on diamond substrates in dissipating heat generated during the optical pumping process (Li et al., 2023). Cheng and colleagues discovered that by altering the encapsulation of the laser bar position, one can significantly reduce the maximum temperature and thermal resistance of the laser (Cheng et al., 2024). Yu introduced a novel fluid rotating microchannel design that facilitates the exchange between upper and lower sections and the mixing of hot and cold sections to enhance heat exchange (Fan et al., 2024). Nakhchi and his team explored the impact of aqueous nanofluids and the geometric parameters of the heat exchanger on its heat exchange capacity. They found that the characteristics of fins alter the fluid flow patterns, while nanoparticles enhance the thermophysical properties of the working fluid, both contributing to improved heat transfer (Nakhchi et al., 2020). Phillips proposed a model for thermal and fluid performance in heat sinks, which significantly enhances their heat dissipation capabilities (Phillips et al., 1998). Deng and colleagues optimized the structure of microchannels in heat sinks using orthogonal tests, which further improved the heat dissipation performance of these microchannel heat sinks (Xiang et al., 2022). Polenz et al. (2021) determined that variations in thermophysical properties significantly enhance the performance of components. Lv and his team employed a topology optimization method to confirm the temperature uniformity and thermal performance of their model (Lv et al., 2018). Qu demonstrated that the conventional Navier-Stokes equations and energy equations can adequately predict the fluid flow and heat transfer characteristics in microchannel heat sinks (Qu et al., 2002). Khan utilized CFD analysis to show that nanofluids exhibit superior overall heat transfer performance (Khan et al., 2019). Beauvais enhanced the design of a liquid-gas heat exchanger fin, and the application of this technique has significantly boosted the performance of the radiator fins (Beauvais et al., 1965). Maghrabie conducted experiments showing that hexagonal ZnO/water nanofluids are more effective than SiO2 nanofluids in improving the thermal performance of automotive radiators (Maghrabie et al., 2022). Vinoth analyzed the heat transfer and flow characteristics of microchannel radiators with slanted fins measuring 48 × 80 mm^2 and found that trapezoidal cross-sections perform better, achieving heat transfer rates that are 8.5% and 10.3% higher than those of square and semicircular cross-sections, respectively (Vinoth, et al. 2018). Xu investigated the thermal and hydraulic performance of microneedle finned radiators, noting that these radiators include enhancements in heat transfer and penalties in pressure drop (Xu et al., 2018).

Subramanian and colleagues found that radiators with

improved hexagonal finned microchannels outperform those with plate-finned microchannels (Subramanian et al., 2019). Xia reported that an optimized design increases the Nusselt number by 53.28% and reduces the voltage drop by 40.89% compared to a conventional microchannel heat sink (Xia et al., 2023). Zeng and colleagues developed unique inline and staggered open-ring pin-finned microchannel heat sinks, with the inline and staggered configurations increasing the Nu by 56–220% and 77–260%, respectively, compared to conventional rectangular microchannels (Zeng et al., 2021). Wu observed that the inlet velocity significantly influences the flow and heat transfer performance. Simulations showed that increasing the velocity from 1 m/s to 9 m/s raised the pressure drop by a factor of 65 and enhanced the heat transfer coefficient by approximately 74.35% (Wu et al., 2022). Peng and collaborators found that MJMC with a greater number of jets, wider outlets, and smaller ratios of fin width to channel width exhibited superior cooling performance (Peng et al., 2020). Additionally, Jiang and team introduced an alternative heat transfer mechanism in their design, which notably improved temperature uniformity by increasing the heat transfer coefficient by 45.1%, reducing the pressure drop by 73.8%, and enhancing the coefficient of performance by 123.1%. This was achieved with a heat flow density as high as 2,677 kW/m^2, a significant improvement over conventional co-flow designs (Jiang et al., 2020). Hu conducted empirical studies on the performance of RBLCP, investigating the effects of bending, runner shape, flow rate, and heating power. He discovered that bending had a minimal impact on heat transfer performance (Hu, et al. 2023). An and colleagues mimicked renal microchannels in their design of a hybrid power lithium-battery thermal management system. At an ambient temperature of 303.15 K and a composite phase-change material mass fraction of approximately 40%, they regulated the maximum temperature between 310.28 K and 309.99 K (An et al., 2022). Liu and his team developed a bionic wing-vein channel cooling plate. This cooling plate, featuring bionic wing channels, not only reduced the maximum temperature and temperature differential of the battery pack but also decreased the pressure loss and energy consumption within the flow channels (Liu et al., 2022). Lastly, Li and associates designed a bionic vascular structure for the liquid-cooled plate of power batteries, discovering that the tube spacing, plate thickness, and inner tube turning radius significantly affect the heat dissipation capabilities of the liquid-cooled plate (Li et al., 2022).

From the discussion above, it becomes clear that to enhance heat dissipation, the structural design of heat sinks, boundary conditions, and the physical properties of the working medium can all be optimized. Nevertheless, practical design continues to face a multitude of challenges. Firstly, the configuration of microchannels—whether arranged in parallel or staggered—can improve heat dissipation to some degree but comes with inherent limitations. In parallel configurations, a phenomenon known as 'short-circuiting' may occur, where the fluid preferentially flows through certain channels, leaving others with insufficient flow. On the other hand, while staggered configurations may promote better fluid mixing, they could also result in increased pressure losses and might not completely resolve the issue of uneven heat dissipation. Secondly, the fluid dynamics within microchannels are prone to instability due to a range of factors. Given the diminutive size of these channels, the effects of surface tension are pronounced, potentially leading to the formation and movement of liquid columns or bubbles. This phenomenon can cause fluctuations in flow and localized deterioration in heat transfer, thereby leading to inconsistent heat dissipation and reduced uniformity across the system. Thirdly, the challenge of achieving a uniform distribution of fluid to each microchannel in microchannel heat dissipation systems is significant and difficult to overcome in practical applications. Fourthly, the distribution of the heat load from cooled objects, such as contemporary electronic devices, is increasingly complex. Such devices often feature multiple heat sources with each source varying significantly in power and heat flow density. As a result, microchannel heat sink systems face formidable challenges in achieving precise heat dissipation matching under these varying conditions. It is crucial to acknowledge that temperature non-uniformities can cause deformations in the heat sink, which might damage the resonant cavity structure of semiconductor lasers. Such deformations can alter the length of the resonant cavity, thereby changing the conditions necessary for the round-trip propagation of light within the cavity. This alteration can lead to a decrease in laser oscillation efficiency and a reduction in output power. The deformations caused by temperature variations produce tensile and compressive stresses in the active region of the laser. Tensile stress is known to decrease the bandgap width, resulting in a shift of the emission wavelength towards longer wavelengths. Conversely, compressive stress increases the bandgap width, shifting the emission wavelength towards shorter wavelengths. Additionally, such deformations may reduce the coupling efficiency between the active region and the resonant cavity, thereby impairing some lasers' ability to effectively participate in the oscillation process, which in turn can impact the output power.

To address these complex issues, this study proposes a novel bionic leaf heat dissipation channel, inspired by the biological characteristics of leaf veins. By exploring the biological structural characteristics of leaf veins and employing bionics and fractal theory, a variety of multi-channel heat dissipation structures are developed. Finite element analysis and numerical studies are conducted on these structures to analyze their heat dissipation mechanisms and optimize their performance in terms of heat dissipation.

2. MATERIALS AND METHODS

2.1 COMPUTATIONAL METHOD

2.1.1 Fluent Numerical Simulation Method

The flow of fluid in the intercooler adheres to the laws of mass, momentum, and energy (John, 2007):

$$\begin{cases} The\ mass\ -\ conservation\ equation: \\ \quad \frac{\partial \rho}{\partial t} + \nabla(\rho v) = 0 \\ The\ momentum\ -\ conservation\ equation: \\ \quad \rho \frac{dv}{dt} - \rho F - dvP = 0 \\ The\ energy\ conservation\ equation: \\ \rho c_P \frac{\partial T}{\partial t} + \rho c_p (V\nabla)T = \frac{D_P}{D_t} + \nabla(k\nabla T) + \Phi \end{cases} \quad (1)$$

Where Equation (1) defines h1 as the specific enthalpy of the fluid, represents the body force per unit volume, λ denotes the thermal conductivity, Sh is the heat source within the fluid, divP is the divergence of the stress tensor per unit volume, and ϵ\epsilonϵ is the dissipation function.

Dimensionless variables are introduced as follows:

$x_1^* = \frac{x_1}{L_0}$, $u_1^* = \frac{u_1}{U_0}$, $t^* = \frac{t}{t_0}$, $p^* = \frac{p}{p_0}$, $T^* = \frac{T}{T_0}$, $f^* = \frac{f}{g_0}$,$\rho^* = \frac{\rho}{\rho_0}$, $\mu^* = \frac{\mu}{\mu_0}$, $k^* = \frac{k}{k_0}$.

By substituting the dimensionless functions $\rho = \rho_0\rho^*$, $t = t_0 t$, $V = V_0 V^*$, and $\Delta = \frac{1}{L_0}\Delta^*$, we perform a dimensionless treatment to derive Equation (2):

$$\left(\frac{L_0}{t_0 U_0}\right)\frac{\partial \rho^*}{\partial t^*} + \nabla^* \cdot (\rho^* V^*) = 0 \quad (2)$$

Further substitution $= \rho_0\rho^*$, $t = t_0 t$, $V = V_0 V^*$, $f = g_0 f^*$,$\tau = \frac{\mu_0 U_0}{L_0}$,$p = p_0 p^*$,$\tau = \frac{\mu_0 U_0}{L_0}$ results in Equation (3).

$$\frac{L_0}{U_0 t_0}\frac{\partial (\rho^* V^*)}{\partial t^*} + \nabla^* (\rho^* V^* V^*) = \frac{g_0 L_0}{U_0^2}\rho^* f^* - \frac{P_0}{\rho_0 U_0^2}\nabla p^* + \frac{\mu_0}{\rho_0 U_0 L_0}\nabla \tau^* \quad (3)$$

Substituting $\rho = \rho_0\rho^*$,$t = t_0 t$,$V = V_0 V^*$,$T = T_0 T^*$,$p = p_0 p^*$,$c_p = c_{p0} c_p^*$,$\phi = \frac{\mu_0 U_0^2}{L_0^2}\phi^*$ yields Equation (4).

$$\frac{L_0}{t_0 U_0} c_P^* p^* \frac{\partial T^*}{\partial t^*} + c_P^* p^* (V^* \nabla^*) T^* = \frac{\mu_0}{\rho_0 U_0 L_0}\frac{k_0}{c_{p0} u_0}\nabla^* (k^* \nabla^* T^*) + \frac{L_0}{U_0 T_0}\frac{P_0}{\rho_0 c_{P0} T_0}\frac{Dp^*}{Dt} + \frac{\mu_0 U_0^2}{\rho_0 U_0 L_0 c_{P0} T}\phi^* \quad (4)$$

2.1.2 Temperature Uniformity

Temperature uniformity refers to the consistency of temperature distribution within a specified spatial range (Yue L et al., 2024):

$$\theta = \frac{T_{\max} - T_{\min}}{T_{\max}} \quad (5)$$

Where Equation (5) defines θ as temperature uniformity, T_{min} as the minimum shell temperature, and T_{max} as the maximum shell temperature.

2.1.3 REYNOLDS NUMBER

The Reynolds number is a dimensionless quantity used to characterize fluid dynamics, expressed in Equation (6) (Rott, 1990):

$$Re = \frac{\rho \bar{v} d}{\mu} \quad (6)$$

Where Equation (6) specifies ρ as the density of the working medium, $\bar{v}$ as the average velocity, d as the characteristic length of the working channel, and μ as the viscosity coefficient.

2.1.4 Nusselt Number

Nu represents the ratio of convective to conductive heat transfer across a boundary, as shown in Equation (7):

$$Nu = \frac{h_2 d}{k} \quad (7)$$

Where Equation (7) identifies h_2 as the convective heat transfer coefficient, d as the characteristic length, and k as the thermal conductivity. The relationship between total heat dissipation and the convective heat dissipation

coefficient is given by Equation (8):

$$Q = hA(T_f - T_w) \quad (8)$$

Where Equation (8) defines Q as the total heat dissipation and A as the heat dissipation area, T_f is the average temperature of the shell, and T_w is the average temperature of the working medium.

When the total heat dissipation Q equals the maximum heat dissipation of the radiator, we derive Equation (9) from Equations (7) and (8):

$$h = \frac{q_{max}}{A(T_f - T_w)} \quad (9)$$

Combining Equations (6) and (9) results in Equation (10):

$$Nu = \frac{q_{max}}{A(T_f - T_w)k} \quad (10)$$

2.2 Modeling

2.2.1 Establishment of the Physical Model

As illustrated in Fig. 1, the semiconductor laser's heat sink channel discussed in this study is inspired by the venation of plant leaves. This channel consists of three main components: the primary channel, the secondary channel, and the heat sink gap. The primary channel features an inlet diameter of 10 mm and outlets each measuring 5 mm in diameter, with a trapezoidal longitudinal cross-section. The dimensions of the trapezoidal cross-section are as follows: the lower base (inlet surface) is 10 mm wide, the upper base is 5 mm wide, and the height is set according to the specific model. The secondary channel is divided into an inlet and an outlet, both with a diameter of 5 mm. The primary channel is angled at 45°, 55°, or 65°, depending on the model. The working medium flows through the inlet channel, traverses the heat dissipation gap, and exits through the outlet channel. The heat dissipation gap is formed by the upper and lower thermal surfaces and thermal blocks. Three models are depicted, denoted as Model I, Model II, and Model III, which differ in their gap heights of 2 mm, 3 mm, and 4 mm, respectively.

2.2.2 Establishment of the Simulation Model

The flow of pure water through a cylindrical conduit is simulated using a three-dimensional fluid-solid interaction model. This model employs the conventional fluid

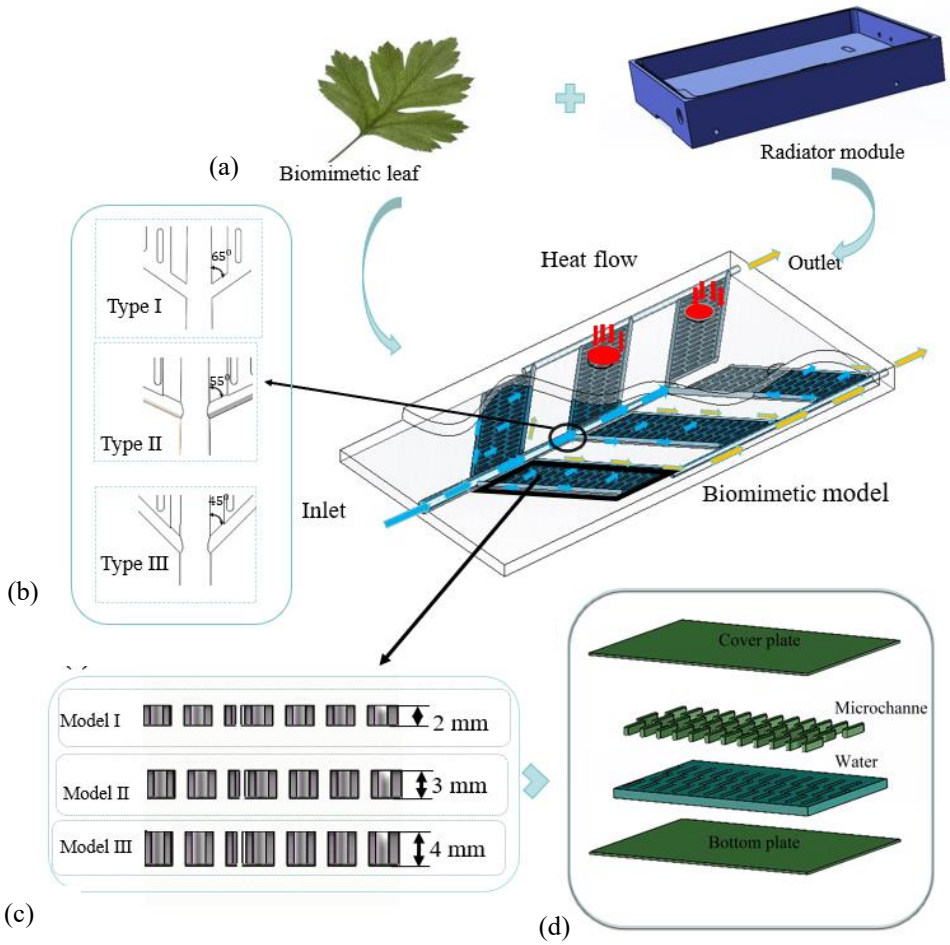

Fig. 1 Model design ideas：(a) Model evolution；(b) Angle of two-stage channel β；(c) Height of heat sink gap H；(d) Diagram of heat dissipation gap composition

dynamics theory, the energy equation, and the k-omega turbulence model. The working fluid is assumed to be a single-phase, incompressible laminar flow, with no consideration given to volumetric forces, heat radiation, or viscosity dissipation. The inlet velocity is uniformly set between 6 m/s and 15 m/s, and the inlet temperature is maintained at 295.15 K. The outlet is unpressurized, indicating an unrestricted flow. The heat source is characterized by a heat flux density. The initial state parameters include an inlet temperature of 295.15 K and an outlet pressure set to zero, ensuring that the flow is not constrained by external pressures. The heat source parameters include a heat flux density of 1.5×10^3 W/m^2 and a constant heat input. All other surface conditions are isothermal. The simulation employs CFD software to address these parameters, as shown in Fig.2, with a convergence residual set to 1×10^{-6}.

2.3 Validation of Mesh Validity

The model's radiator is meshed using a tetrahedral meshing technique, with multi-area meshing applied to simplify computational demands. The mesh size for the radiator's outer shell is set at 4 mm, as depicted in Fig. 3(b), and the mesh size for the runner section is 2 mm, as shown in Fig.3(c).

For the bionic blade, calculations were conducted using 11 different grid cell counts: 337,131; 582,106; 707,477; 882,561; 1,106,698; 1,490,025; 1,980,849; 2,848,398; 2,854,500; 4,646,722; and 8,490,362. The results for the maximum and average water flow velocities at the radiator outlet are presented in Fig.4. Analysis of these results indicates that when the number of grid cells in the computational domain reaches 2 million or more, further increases in grid cell count do not significantly affect the computed values of maximum and average velocities at the radiator outlet. Consequently, the mesh for the computational domain of the physical model has been set to use 1,980,849 discrete grid cells, with a mesh size of 4 mm for the radiator's outer shell and 2 mm for the runner section. The meshing approach used for the design model follows this same methodology.

3. RESULTS AND DISCUSSION

3.1 Effect of Gap Height

In this subsection, we compare the thermal performance of newly designed bionic leaf cooling channels by varying the heat dissipation gap. Three channels, each using different media and featuring different gap heights, were designed to analyze the impact of gap size on thermal performance. The simulations were conducted at a heating temperature of 315.15 K. As shown in Fig.6(a), the average surface temperature of the innovative bionic leaf cooling channel ranges from 295.30 K to 295.50 K,

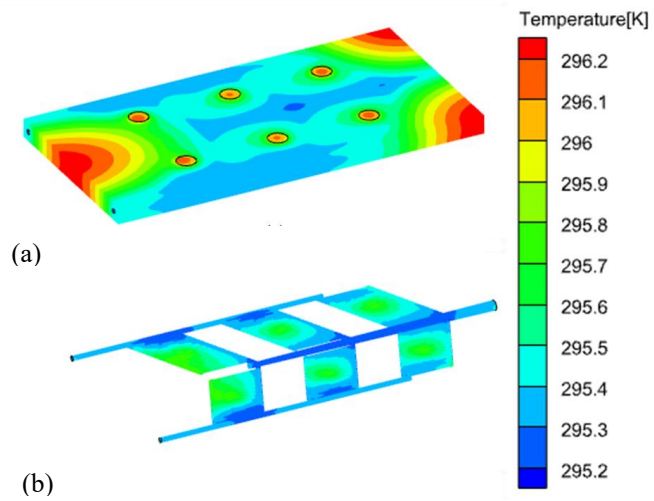

Fig. 2 Simulated Temperature Cloud; (a) Overall temperature cloud; (b) Medium temperature cloud

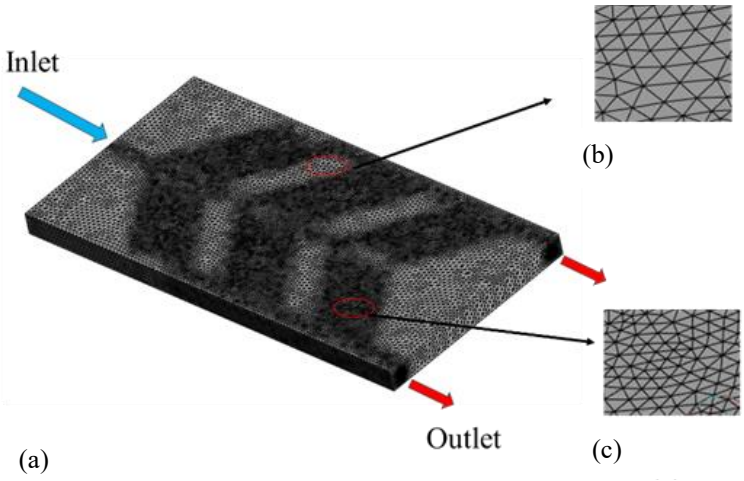

Fig. 3 Mesh generation: (a) Overall model meshing; (b) Grid size 4 mm; (b) Grid size 2 mm

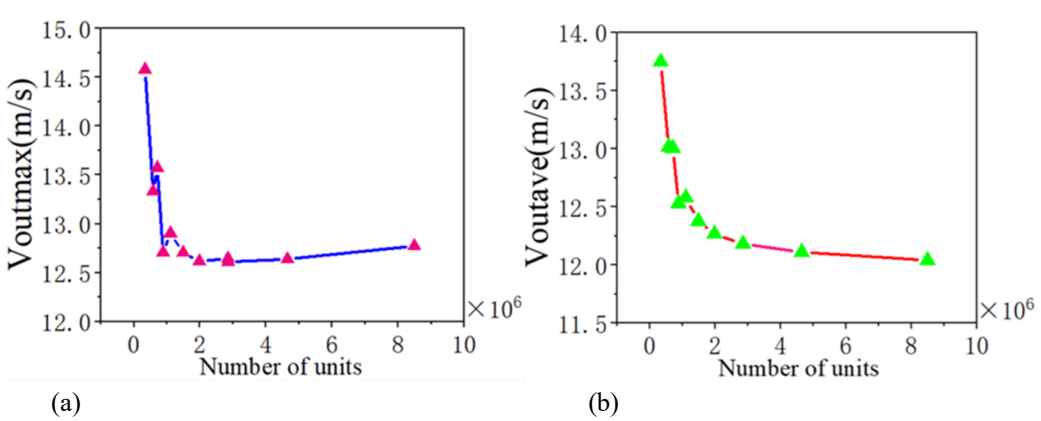

Fig. 4 Grid validity speed verification：(a) Average speed of exports； (b) Maximum exit speed

achieving a minimum temperature reduction of 20 K compared to the heat source. The results indicate that the novel bionic leaf cooling channel significantly lowers the surface temperature. Further investigation reveals a direct correlation between the heat dissipation gap and the surface temperature across the three types of bionic leaf channels. It is observed that an increase in the heat dissipation gap enlarges the contact area between the water flow and the channel shell, which in turn enhances heat removal. It is important to note that the heat generated by the semiconductor laser remains constant. The improved heat dissipation is attributed to increased heat removal, which leads to a decrease in residual heat and enhances dissipation efficiency. For the type I and II models, it has been noted that setting the heat dissipation gap at 4 mm results in decreased dissipation efficiency in the surface channels. Notably, the temperature in the type II model shows a slight increase. This issue can be traced

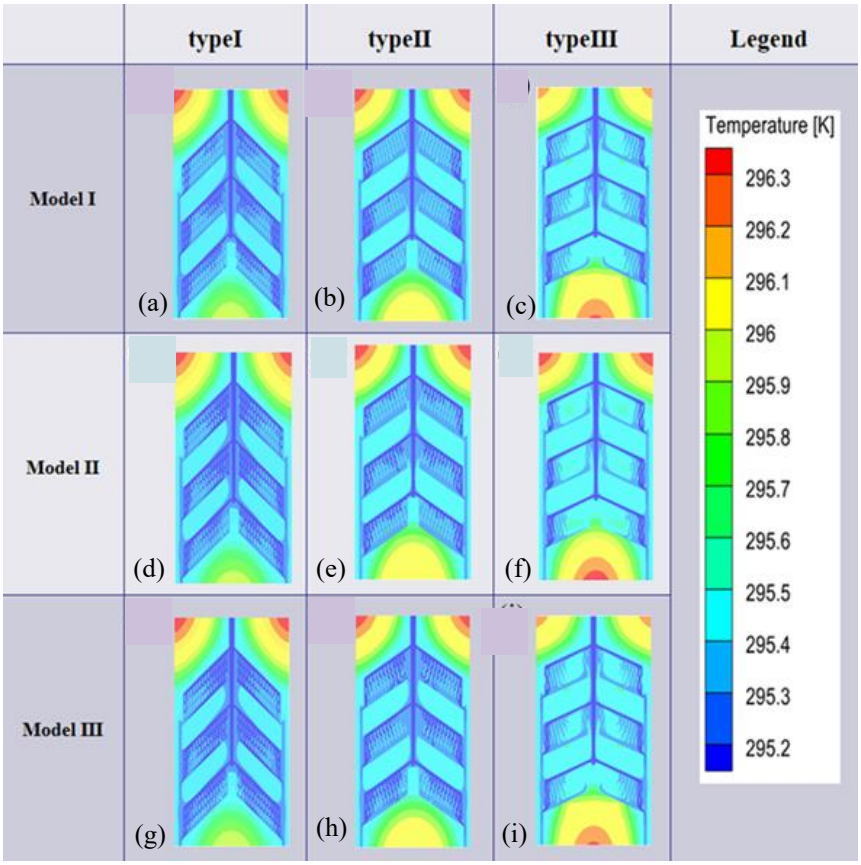

Fig. 5 Temperature cloud maps corresponding to different scales: (a) β=45°,H=2 mm; (b) β=55°, H=2 mm, (c) β=65°, H=2 mm; (d) β=45°, H=3 mm; (e) β=55°, H=3 mm, (f) β=65°, H=3 mm; (g) β=45°, H=4 mm, (h) β=55°, H=4 mm; (i) β=65°, H=4 mm

back to the inadequate angles between the primary and secondary pipes in the type I and II models. If these angles are too small, the working medium is forced to flow more rapidly, leading to the formation and movement of liquid columns or bubbles. These dynamics cause fluctuations in the flow and localized deterioration in heat transfer. Temperature variations corresponding to these observations can be seen in Fig.5.

As illustrated in Fig.6(c), the *Nu* of the heatsink channel is dependent on changes in the heatsink gap. The analysis remains quantitative under constant boundary conditions, with only the structural features undergoing modifications; these alterations closely resemble the original structure. Additionally, *Nu* serves as a valuable metric for evaluating thermal performance. Therefore, this study recommends using Nu to assess the variations in thermal performance attributable to structural modifications. In this subsection, we examine a model with a thermal gap of 2 mm. For this model, Nu values are recorded as 1,371, 1,687, and 1,956, respectively. When the thermal gap is increased to 3 mm, the Nu values escalate by 24.79%, 13.93%, and 10.73%, respectively. Further expansion of the gap to 4 mm results in Nu values of 1,731, 1,897, and 2,265, representing increases of 25.74%, 12.93%, and 15.80%, respectively, compared to the model with a 2 mm gap. However, when these values are compared with the model featuring a 3 mm gap, the increases for the 4 mm gap are 25.74%, 12.48%, and 15.80%, respectively. It is noted that for models of type I and type III, there is a slight increase in *Nu*, whereas for type II, there is a reduction of 1.27%. This decrease can be attributed to the higher water inflow into the gap compared to the secondary channel at a 2 mm thermal gap, where the resistance to water flow is greater, resulting in a lower flow rate through the thermal gap. The flow rate of water on the exterior significantly exceeds that on the interior, which ultimately reduces the heat dissipation effect. On the contrary, at a thermal gap of 3 mm, the resistance to water flowing into the gap significantly increases, which results in an increased measured water flow rate within the gap. This, in turn, substantially enhances the heat dissipation effect. At a thermal gap of 4 mm, although the enhancement in heat dissipation is still evident, it is much less pronounced than at a 3 mm gap. According to the principles of fluid mechanics, an increase in the size of the channel decreases the flow rate of the fluid for a given volume flow rate. The heat dissipation effect is closely related to the convective heat transfer coefficient between the fluid and the wall, and a lower flow rate will reduce this coefficient, leading to a decrease in the heat dissipation capacity.

The purpose of designing the radiator is to lower the operating environment temperature of the laser, thereby enhancing its performance. However, overlooking the impact of temperature differences while reducing the ambient temperature can lead to a decline in performance. This occurs because temperature differences can cause the working surface to deform due to thermal expansion and contraction, which then results in slight changes in the

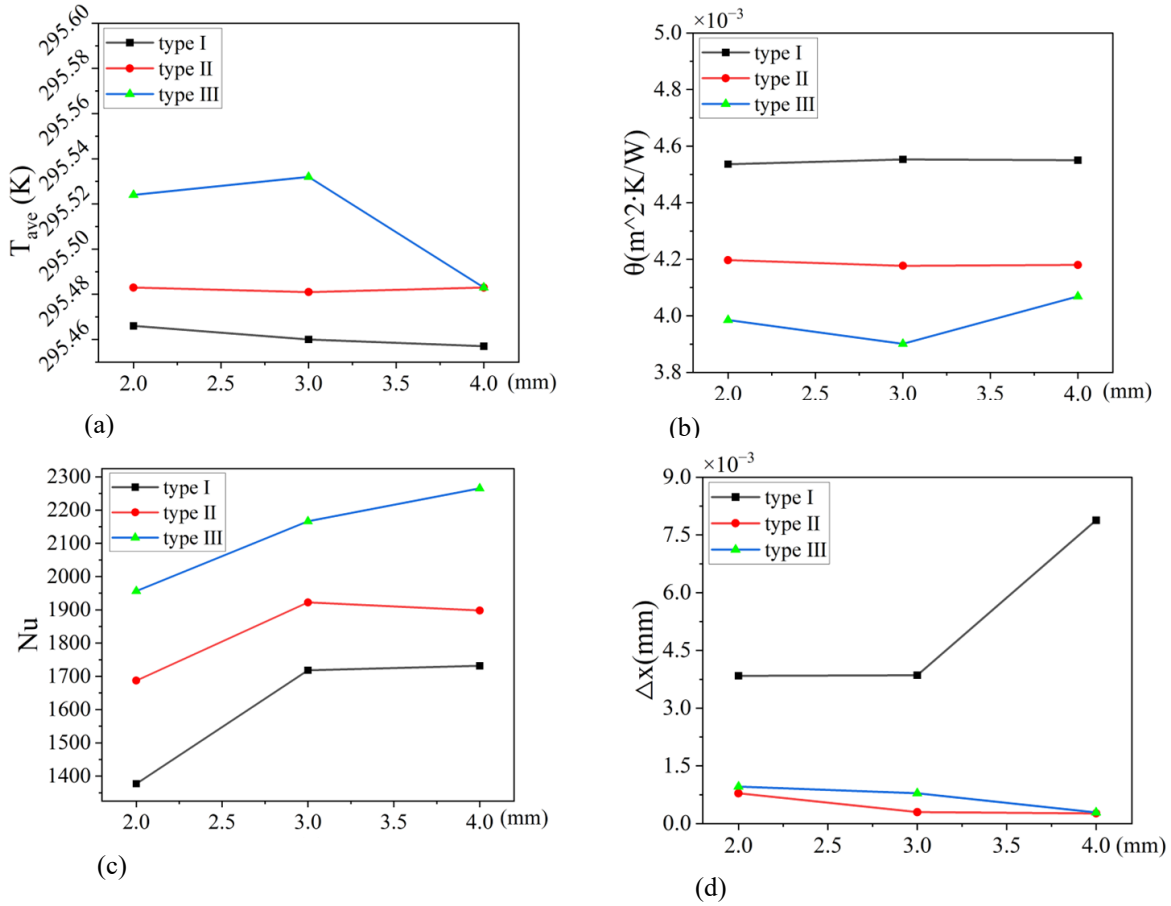

Fig. 6 Change the heat dissipation gap:(a) Average temperature; (b) Temperature uniformity;(c) Model *Nu*; (d) Model deformation amount

angle and position of the two mirrors within the optical resonator. Consequently, the amplification of light is weakened, and errors in frequency selection may occur. As illustrated in Fig.6(b), increasing the cooling gap slightly alters the temperature uniformity, though the change is minimal, and the magnitude of the temperature gradient remains largely unchanged. From Fig. 6(d), it is evident that the deformation is most significant in type I. With a radiator gap of 2mm, the deformation is at its minimum, measuring 0.00384 mm. When the gap is increased to 4 mm, the deformation peaks at 0.00788 mm. type III exhibits the second highest level of deformation, while type II shows the least, with both types having deformation amounts ranging from 0 to 0.00100 mm. The deformation in type I increases, whereas it decreases to varying extents in type II and III. This variation is due to differences in the thermal performance of the internal and external dimensions of the cooling gaps, which lead to temperature differences. Larger temperature differences result in greater deformations. As the cooling gap widens, its heat exchange area expands, the volume of water flowing through it increases, and the rate of heat exchange accelerates. Since type I has a longer longitudinal length than type II and III, its internal and external temperature difference is greater, causing more significant deformation. Additionally, as the cooling gap increases, fluctuations in flow rate also rise. These unstable flow rates can cause variations in the strength of the heat transfer process, affecting the heat dissipation conditions at different points within the microchannel. This, in turn, exacerbates the unevenness of heat dissipation and leads to greater deformation. In summary, when only the height of the radiator gap is adjusted, its Nu will increase, but the improvements in temperature uniformity and model deformation are limited and may even exacerbate these issues. The optimal configuration is for type I to have a cooling gap of 3 mm, type II to have 2 mm, and type III to have 3 mm. This setup achieves the best balance between heat dissipation performance and working efficiency. When type III employs a cooling gap of 3 mm, it demonstrates optimal heat dissipation and minimal model deformation.

3.2 Effects of Angles

In this subsection, we compare the thermal performance of a newly designed bionic leaf cooling channel by varying the angle of its two-stage channel clamp. Temperature serves as the most direct parameter for evaluating the system's performance. The heating temperature for this simulation is maintained at 315.15 K, with boundary conditions consistent with those outlined in section 3.1.1.

Figure 7(a) illustrates how the average temperature on the working surface of the heat dissipation channel in the new bionic blade varies with the clamping angle. The results indicate that the average temperature of the working

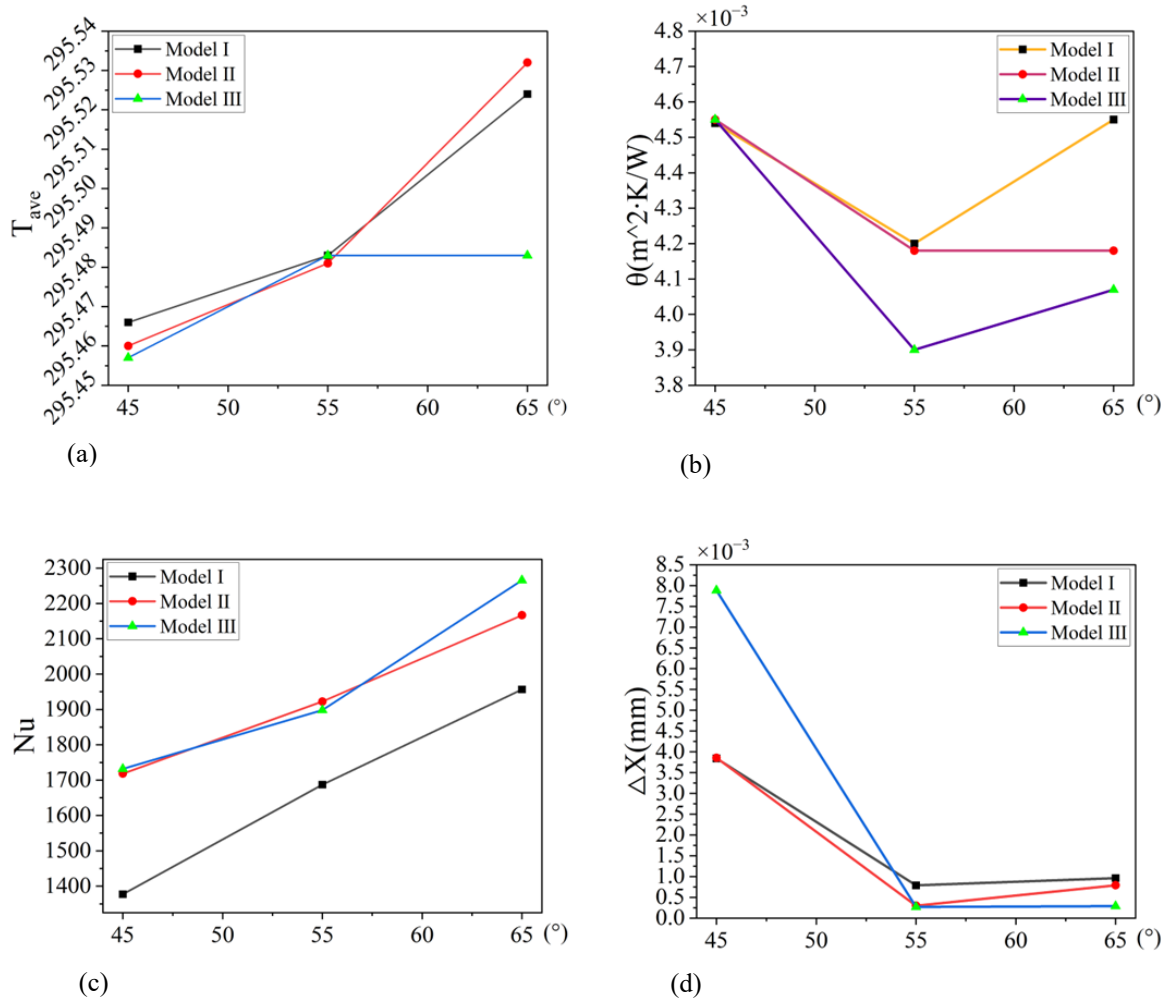

Fig.7 Effect of the angle between the tow channels: (a)Average temperature; (b)Temperature uniformity; (c) Model *Nu*; (d)Model deformation amount

surface increases as the clamping angle widens. This increase is attributed to the fact that at a 45° angle, the longitudinal heat dissipation area of the two-stage channel is larger than that of other channels. Within a given transverse heat dissipation area, this configuration provides the largest heat dissipation area, followed by the 55° angle, with the smallest being at 65°. Consequently, the average temperature rises as the angle increases.

Figure 7(b) explores the impact of the increasing angle on the temperature uniformity across each model. Temperature uniformity can be assessed by examining the size of the temperature gradient, which in turn reveals the extent of local heat dissipation deterioration. The results demonstrate that the model achieves optimal temperature uniformity at a bifurcation angle of 55°. In contrast, the worst uniformity occurs at a 45° angle, indicating a significantly greater deterioration in local heat dissipation at this angle compared to the 55° angle. This finding also helps predict the potential degree of deformation in the model.

The impact of varying the bifurcation angle on the *Nu* is illustrated in Fig.7(c). The analysis method employed here is consistent with that described in Section 3.1. As shown in Fig.7(d), it is evident that the *Nu* increases as the bifurcation angle between the main and secondary pipes widens. A bifurcation angle of 45° serves as a baseline for evaluating each model individually. At a bifurcation angle of 55°, the *Nu* values are 1687, 1922, and 1897, which represent increases of 22.53%, 11.87%, and 10.73% over Models I, II, and III at 45°, respectively. At an angle of 65°, the *Nu* values are 1731, 1897, and 2265, showing enhancements of 42.07%, 26.06%, and 30.84% compared to Models I, II, and III at 45°, respectively. Additionally, these values are 15.95%, 12.70%, and 19.37% higher than the respective models at 55°. Generally, it is observed that *Nu* increases as the bifurcation angle enlarges. As the angle between the two pipe stages increases, the flow speed in the secondary piping accelerates. As depicted in Fig.8, the flow velocity at the radiator gap increases, thereby enhancing the *Nu* as the angle between the stages grows. This enhancement occurs because an increased angle between the two stages of the channel alters the overall resistance of the water flow in the thermal gap. This alteration reduces the water flow velocity in the secondary piping, increases the flow speed in the thermal gap, and strengthens the impact of the water flow on the heat sink block. Consequently, the rate of heat exchange

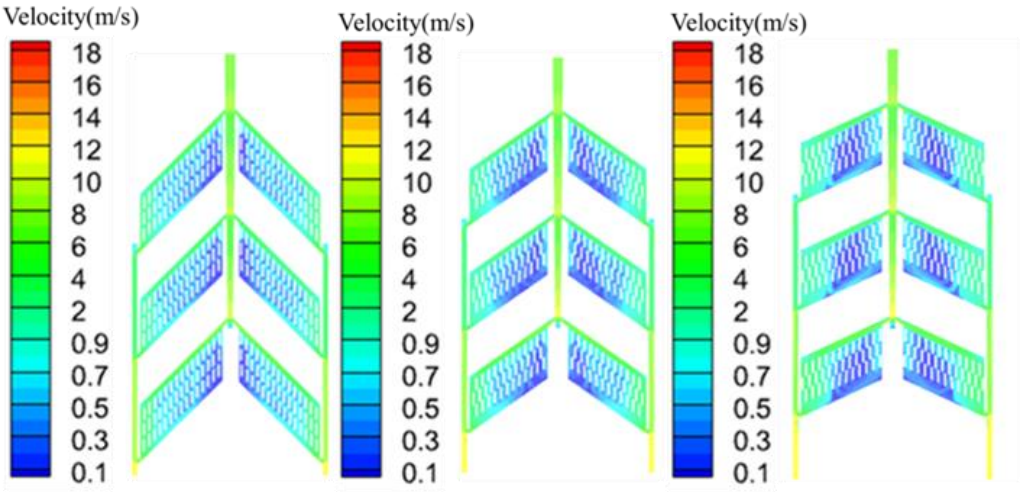

(a) (b) (c)

Fig.8 Speed of each part of the heat dissipation gap at different angles: (a) Speed of each part of the heat dissipation gap at 45°; (b) Speed of each part of the heat dissipation gap at 55°; (c) Speed of each part of the heat dissipation gap at 65°

on the wall surface intensifies, leading to improved overall heat dissipation. The underlying physical mechanism involves an increase in flow velocity, which boosts convective heat transfer within the microchannel. According to heat transfer principles, as flow velocity escalates, the relative motion between the fluid and the wall surface of the microchannel increases. This results in a thinner boundary layer and reduced thermal resistance. Consequently, heat is transferred more efficiently from the microchannel wall to the fluid, enhancing heat dissipation efficiency.

Figure 7(d) illustrates the deformation caused by thermal expansion and contraction across different models. The data indicate that deformation is most significant when the angle is 45 degrees. Models I and III exhibit the least deformation, showing little variation when the angle increases to 55 degrees and 65 degrees. In contrast, Model II demonstrates minimal deformation at an angle of 55 degrees, but its deformation increases as the angle reaches 65 degrees. This behavior correlates with the velocity of flow in the channel and heat sink gap, which rises with increasing angle. Consequently, more heat is removed, enhancing the heat dissipation effect. Additionally, as the angle widens, the longitudinal heat dissipation area of the heat sink gap becomes larger and more focused, which centralizes the cooling effect on the heat source and minimizes heat transfer within the model. These factors contribute to a smaller temperature gradient and thus less deformation. Temperature variations are depicted in Fig. 5.

In summary, increasing the inlet flow rate consistently elevates the *Nu*, although the overall temperature remains unchanged. At a Reynolds number (Re) of 20,000, the expansion of low-temperature regions does not persist. Therefore, at this flow rate, *Nu* alone is insufficient to assess the cooling effect; instead, it should be evaluated in conjunction with the temperature distribution. Moreover, an increase in the inlet water flow rate enhances the overall water flow distribution and improves heat dissipation. However, this also increases the disparity in cooling performance across different parts, resulting in a higher temperature gradient and more pronounced deformation.

Table 2 Optimal solution model

Kind	Heat dissipation gap(mm)	Two level channel angle (°)
Kind I	2	65
Kind II	3	55
Kind III	4	65

3.3 Influence of Inlet Velocity

By modifying the height of the heat sink gap and the angle of the two-stage channel, we analyze the effects of these structural parameters on both thermal and operational performance, ultimately selecting the optimal configurations. These configurations have been renamed as follows: Model I and Model III are termed Kind I and Kind III, respectively, at a pinch angle of 65°, and Model II, at 55°, is referred to as Kind II, as shown in Table 2.

In this subsection, the inlet velocity of the water is set at 6 m/s, 9 m/s, 12 m/s, and 15 m/s. At these velocities, the Re significantly exceeds 4,000, indicating that the flow regime is turbulent. Turbulence enhances heat dissipation efficiency by increasing both fluid mixing and heat transfer. It disrupts the laminar flow structure of the fluid, leading to more uniform heat distribution and, consequently, improved cooling effects. Moreover, higher turbulence levels intensify collisions between fluid masses, accelerating energy exchange and benefiting heat transfer. However, turbulence can also increase the mixing of the fluid and create unevenness in heat transfer, which might, to some extent, decrease the overall efficiency of heat dissipation. Additionally, increasing the inlet water flow velocity to enhance the velocity distribution of water flows both internally and externally within the thermal gap further boosts heat dissipation. The three optimal solutions presented in Table 2 are further refined accordingly.

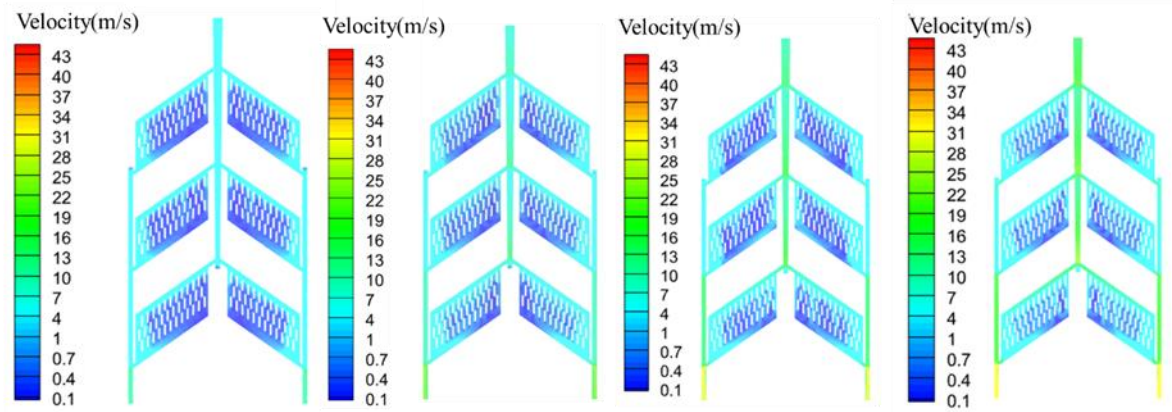

Fig. 9 Velocity clouds at different *Re*: (a) *Re*=7×10^3; (b) *Re*=1.1×10^4; (c) *Re*=1.4×10^4; (d) *Re*=2×10^4.

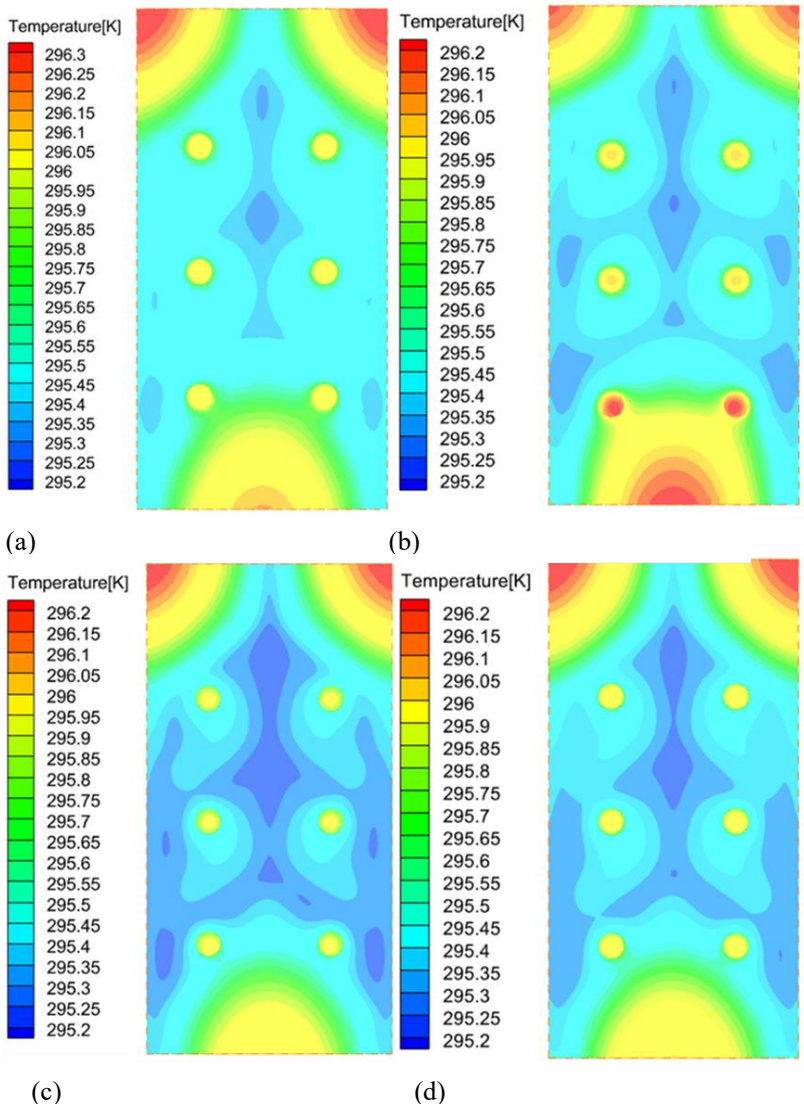

Fig. 10 Temperature cloud map of Kind II working surface at different *Re*: (a) *Re*=7×10^3; (b) *Re*=1.1×10^4; (c) *Re*=1.4×10^4; (d) *Re*=2×10^4

As shown in Fig. 9, the velocity cloud of type II exhibits a significant increase in the velocity distribution of water both within and beyond the thermal gap, following an increase in the inlet flow rate. This leads to a marked improvement in the heat dissipation capabilities of the thermal gap. Additionally, as illustrated in Fig. 10, there is a gradual expansion in the extent of the low-temperature area within its temperature cloud as the rotational speed

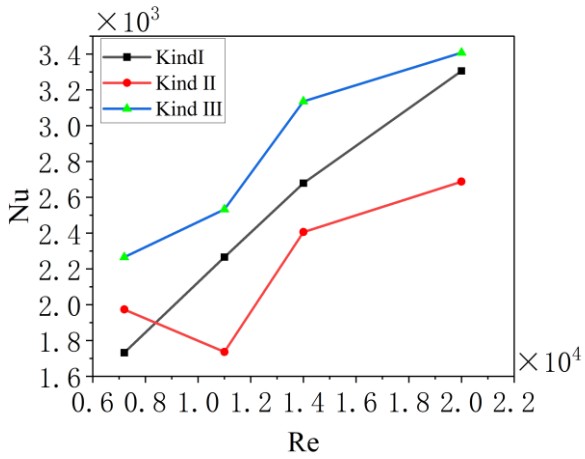

Fig. 11 Influence of *Re* on *Nu*

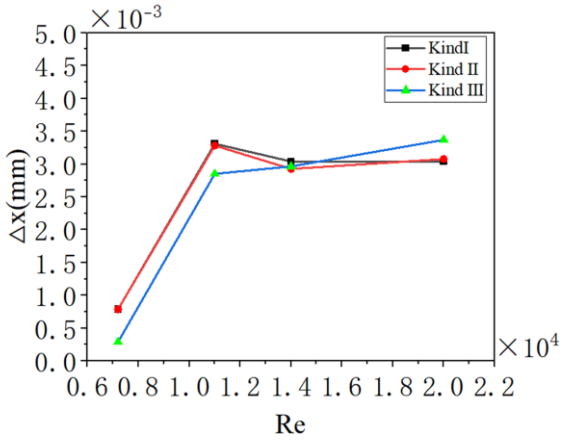

Fig. 12 Influence of *Re* on deformation

increases. This observation suggests a substantial enhancement in the heat dissipation effect. However, the range of its Nu values varies. As depicted in Fig. 11, the Nu values for type I, type II, and type III are 1,731, 1,972, and 2,265 respectively, at a Re of 7,000. When the Re value increases to 20,000, the corresponding Nu values rise to 3,305, 2,686, and 3,407, representing increases of 90.96%, 36.19%, and 50.41% respectively compared to the Re value of 7,000. This trend is attributed to several factors. Firstly, as the Re value increases, it enhances the irregular motion and mixing within the fluid, speeding up the exchange of fluid at the heat transfer wall with the main flow. Secondly, the increase in Re also intensifies the disturbance of the fluid, resulting in the continuous disruption and thinning of the thermal boundary layer, which leads to an increase in the convective heat transfer coefficient and improved heat transfer. Thirdly, the swirling effects of turbulence improve the filling of all corners of the channel by the fluid, enlarging the contact area with the wall compared to laminar flow. This increases the volume of fluid involved in heat exchange and, consequently, boosts the heat transfer capacity. However, as shown in Fig. 10(d), this expansion is not sustained; rather, it undergoes a contraction. This phenomenon is attributed to the presence of counterflow in the opposite direction when the flow velocity becomes excessively high and the water interacts with the heat sink block. This counterflow results in a reduction of flow velocity (as shown in Fig.9) and a decrease in collision intensity, ultimately leading to a reduced heat dissipation effect. The impact of increasing the Re value on Nu is further exemplified in Fig.10, which shows that with an increase in Re value, the heat transfer effect is enhanced and the wall temperature is significantly reduced.

Figure 12 illustrates the impact of increasing the Re on deformation. As shown in Fig.11, when the Reynolds number rises from 7×10^3 to 1.1×10^4, the deformation increases sharply, reaching 0.00350 mm. However, when the Re reaches or exceeds 1.1×10^4, the deformation fluctuates within a narrow range. This fluctuation occurs because the increase in inlet flow velocity leads to a greater velocity difference across the thermal gap's inner and outer sides. Consequently, this difference affects the thermal performance of these sides, increasing the temperature disparity and exacerbating the deformation. Additionally, an excessively high flow velocity can cause unstable fluid flow within the channel, inducing vortex formation. This phenomenon disrupts the uniformity of heat dissipation, further intensifying the deformation.

In summary, increasing the inlet flow rate consistently results in a rise in the *Nu*, yet the overall temperature does not decrease. When the Reynolds number reaches 20,000, the expansion of the low-temperature region ceases. Therefore, at this point, the Nusselt number alone is insufficient to evaluate the cooling effect. Instead, it should be assessed in conjunction with the temperature distribution, referred to as the "temperature cloud." On another note, increasing the inlet water flow rate enhances the distribution of water flow and improves the heat dissipation effect. Simultaneously, this adjustment leads to a greater disparity in the cooling performance among different parts, and the temperature gradient increases, which intensifies the degree of deformation.

4. EXPERIMENTATION

The main purpose of this experiment is to verify whether the radiator has heat dissipation performance and the authenticity of the simulation. The experimental equipment in this experiment is composed of a water tank, an inlet water pipe, a stopcock, a heat source, an electric source, a radiator, a flowmeter, an outlet water pipe, and a thermometer as shown in Fig.13. Among them, the water tank provides a stable water flow. The temperature of the water flow is 295.05K, and the flow rate is 15 L/min. The electric source provides a stable electric current, which converts the 220V alternating current into 24V direct current. The heat source provides stable heat, which is a 20W MCH high-temperature ceramic heating plate. The included angle between the two pipes of the radiator model is 45°, and the heat dissipation gap is 2mm. The flowmeter can measure the flow rate of the water outlet, and the thermometer measures the temperature of the water outlet. After starting the water tank, the temperature shown on the thermometer reaches stability after 5 minutes. The temperature shown is 296.55K, and the water temperature has increased by 0.5K compared with the inlet temperature. The maximum outlet temperature of the simulation results of the radiator with the same parameters

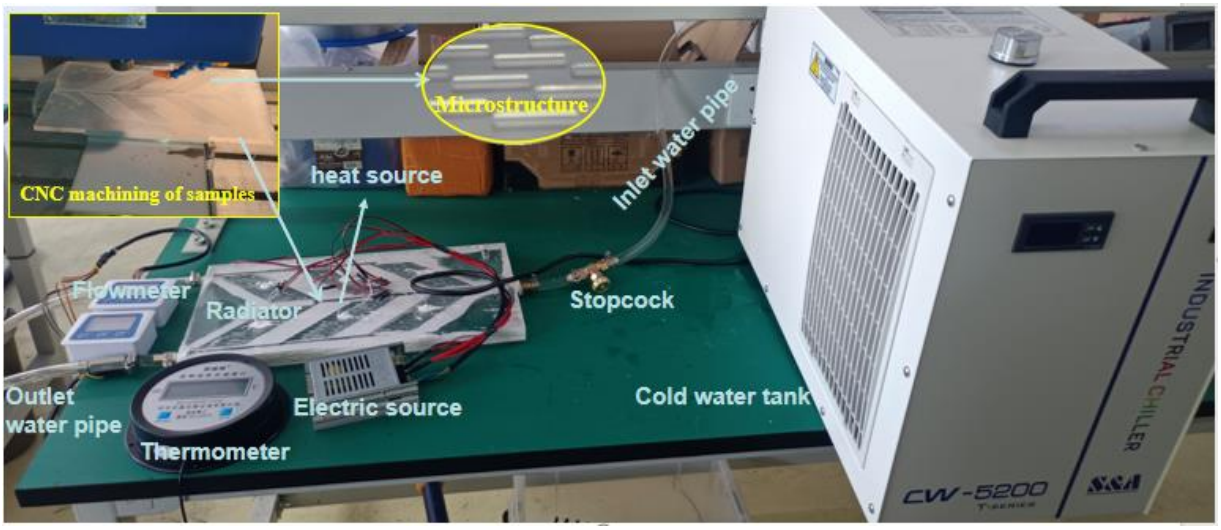

Fig. 13 Heat dissipation experiment

is 296.494K, and the minimum temperature is 295.149K. Due to factors such as the accuracy of the thermometer, model errors, and the temperature error of the water flow at the outlet of the cold water tank, there is a certain gap between the experimental data and the simulation data. However, the results obtained are the same, so the simulation results are consistent with the experimental results. The semiconductor laser radiator designed in this paper has good heat dissipation performance, and at the same time, it verifies the authenticity of the simulation in this paper.

5. CONCLUSION

In this study, we have explored the integration of bionics with fractal theory to create a novel bionic leaf heat dissipation channel, inspired by the transformed biological characteristics of leaf veins. The findings from our simulation analysis and numerical study lead us to the following conclusions:

(1) When considering a fixed overall height, the height of the heat sink gap is the sole variable adjusted. A larger gap results in more effective heat dissipation within the allowable parameters. Specifically, for type III, when the heat sink gap is set to 4 mm, the *Nu* reaches its highest at 2,265. As the gap height increases, type I shows the most significant improvement in *Nu*, which escalates from 1,377 to 1,731, marking a maximum increase of 25.74%. However, this configuration also exhibits the least temperature uniformity and the most deformation.

(2) Modifying the angle between the primary and secondary channels of the microchannel is shown to be an effective method for enhancing heat dissipation. At a heat source temperature of 315.15 K, the post-dissipation shell temperatures are recorded at 295.40 K and 295.54 K, respectively, achieving a cooling effect of at least 20 K. The improvement in modeled heat dissipation is notably substantial as the angle increases. Model I's *Nu* increases from 1,377 to 1,956, a 42.07% rise, and Model III attains a maximum *Nu* of 2,265 at a 65° angle. This adjustment also significantly enhances the temperature uniformity and reduces deformation in the model.

(3) Increasing the water flow inlet velocity also enhances heat dissipation performance. type III shows the most notable improvement at a Re of 20,000, where *Nu* peaks at 340. type I displays the greatest enhancement, with *Nu* increasing from 1,731, to 3,305, an increase of 90.93%. However, higher water flow inlet velocities exacerbate the velocity differences inside and outside the heat dissipation gap, leading to significant performance disparities and increased deformation of the model.

(4) Turbulence plays a crucial role in the heat dissipation of heat sinks. Enhanced heat dissipation effects are observed at *Re* values of 7,000, 11,000, and 16,000. However, the heat dissipation effect diminishes when Re reaches 20,000. At certain Re values, turbulence effectively boosts heat dissipation.

(5) The laser radiator designed in this study can be configured with either a single fin or multiple fins and is capable of dissipating heat from single or multiple heat sources, such as integrated high-power LEDs, high-energy-consuming CPUs, and power integrated circuits.

(6) The microchannel heat sink of the semiconductor laser designed in this paper has good heat dissipation performance and can reduce its temperature by about 0.5 degrees.

ACKNOWLEDGEMENTS

The Science and Technology Research Project of the Education Department of Jilin Province (JJKH20251095KJ) and Changchun University PhD Fund (2024JBE01L02) supported the work.

CONFLICT OF INTEREST

The authors declare no conflict of interest.

AUTHORS CONTRIBUTION

Zhenhua Hou Providing research ideas, program design, and data analysis. **Zhenfu Zhou** Manuscript data analysis, writing, graphing, and data collection. **Ke Zhang**

Data collection, data analysis, and literature search. **Yi Ji** Data collection. **Yuxiang Zheng** Study design. **Libo Wang** Research ideas, program design, data analysis. **Shijie Li** Data analysis. All authors have read and agreed to the published version of the manuscript.

REFERENCE

An, Z. G., Zhang, C. J., Gao, Z. Y., Luo, Y. S. & Dong, Y. (2022). Heat dissipation performance of hybrid lithium battery thermal management system using bionic nephrolepis micro-channel. *Applied Thermal Engineering, 217*, 119127. https://doi.org/10.1016/j.applthermaleng.2022.119127

Beauvais, F. N. (1965) An aerodynamic look at automotive radiators. *SAE Technical Papers*.

Cheng, L., Sun, H. Q., Dai, X. J., & B. X. Wei (2024). Optimization of heat-dissipation structure of high-power diode laser in space environments. *Micromachines, 15*(8), 968. https://doi.org/10.3390/mi15080968

Hu, H. Z., Chen, C. M., Li, C., & M. Q. Pan (2023). Experimental investigation of roll bond liquid cooling plates for server chip heat dissipation. *Applied Thermal Engineering,226*, 120284. https://doi.org/10.1016/j.applthermaleng.2023.120284

Jiang, X. C., Zhang, S. W., Li, Y. J., & Pan, C. (2020). High performance heat sink with counter flow diverging microchannels. *International Journal of Heat and Mass Transfer, 162*, 120344. https://doi.org/10.1016/j.ijheatmasstransfer.2020.120344

John, D. (2007). *Fundamentals of computational fluid dynamics and its applications.* Beijing: Machinery Industry Press.

Khan, T. A., & Ahmad, H. (2019). CFD-based comparative performance analysis of different nanofluids used in automobile radiators. *Arabian Journal For Science And Engineering, 44*, 5787-5799. https://doi.org/10.1007/s13369-019-03750-9

Li, S., Li, J., Xu, H., Ma, J., & Peng, H. (2020). Numerical study on heat transfer and flow characteristics of novel microchannel heat sinks. *International Journal of Thermal Sciences, 176*. 107535. https://doi.org/10.1016/j.ijthermalsci.2022.107535

Li, B., Wang, W. H., Bei, S. Y., & Z. Q. Quan (2022). Analysis of heat dissipation performance of battery liquid cooling plate based on bionic structure. *Sustainability, 14*(9), 5541. https://doi.org/10.3390/su14095541

Li, C. Q., Huang, Y. L., Shang, & H. Y. Huang (2020). Study on the flow and heat dissipation of water-based alumina nanofluids in microchannels. *Case Studies in Thermal Engineering,, 22*, 100746. https://doi.org/10.1016/j.csite.2020.100746

Li, H. G., Z. Hou, Y. F. Wei, R. F. Zhao, T. Ji, W. Y. Wang, R. Wen, K. B. Zheng, S. W. Yu and Y. X. Cui (2023). Efficient heat dissipation perovskite lasers using a high-thermal-conductivity diamond substrate. *Science. China Materials, 2023, 66*(6), 2400-2407. http:// doi.org/10.1007/s40843-022-2355-6

Liu, X., Sun, A., Tian, C. (2022). Research on liquid cooling and heat dissipation of lithium-ion battery pack based on bionic wings vein channel cold plate. *ESST, 11*(7), 2266. https://doi.org/10.1016/j.ijheatmasstransfer.2021.122178

Lv, Y., & Liu, S. (2018). Topology optimization and heat dissipation performance analysis of a micro-channel heat sink. *Meccanica, 53*(15), 3693-3708. https://doi.org/10.1007/s11012-018-0918-z

Ma, C. B., Sun, Y. N., Wu, Y. J., Zhang, Q. Z., Wang, Y., & G. F. Ding (2023). A bio-inspired fractal microchannel heat sink with secondary modified structure and sub-total-sub fluid transmission mode for high heat flux and energy-saving heat dissipation. *International Journal of Heat and Mass Transfer, 202*, 123717. https://doi.org/10.1016/j.ijheatmasstransfer.2022.123717

Maghrabie, H. M., & Mousa, H. M. (2020). Thermal performance intensification of car radiator using SiO2/water and ZnO/water nanofluids. *Journal Of Thermal Science And Engineering Applications*, *14*(3), 034501. https://doi.org/10.1115/1.4051382

Nakhchi, M. E., & Esfahani, J. A. (2020). CFD approach for two-phase CuO nanofluid flow through heat exchangers enhanced by double perforated louvered strip insert. *Powder Technology, 367*, 877-888. https://doi.org/10.1016/j.powtec.2020.04.043

Peng, M., Chen, L., W. T. Ji, & Tao W. Q. (2020). Numerical study on flow and heat transfer in a multi-jet microchannel heat sink. *International Journal of Heat and Mass Transfer*, *157*, 119982. https://doi.org/10.1016/j.ijheatmasstransfer.2020.119982

Phillips R. J. (1988). Microchannel heat sinks. *The Lincoln Laboratory Journal, 1*(1), 31-48.

Polenz, S., Kolbe, C., Bittner, F., López, E., Brückner, F., & Leyens, c. (2021). Integration of pure copper to optimize heat dissipation in injection mould inserts using laser metal deposition. *The Journal of Laser Applications,* 33(1). https://doi.org/10.2351/7.0000303

Qu, W., & Mudawar, I. (2002). Experimental and numerical study of pressure drop and heat transfer in a single-phase micro-channel heat sink. *International Journal of Heat and Mass Transfer*, *45*(12), 2549-2565. https://doi.org/10.1016/S0017-9310(01)00337-4

Rott, N. (1990). Note on the history of the Reynolds number. *Annual Review of Fluid Mechanics, 22(1)*, 1-12.

Song, M. J., Z. Y. Jiang, C. B. Dang, Y. Y. Jiang, J. Shen, X. Y. Luo (2020). Mathematical modeling investigation on flow boiling and high efficiency heat dissipation of two rectangular radial microchannel heat exchangers. *International Journal of Heat and Mass Transfer, 190*, 122736. https://doi.org/10.1016/j.ijheatmasstransfer.2022.122736

Subramanian, S., Sridhar, K. S, & Umesh, C. K. (2019). Experimental investigation of microchannel heat sink with modified hexagonal fins. *Journal of Applied Fluid Mechanics, 12(3)*, 647-655. https://doi.org/10.1115/1.4040956

Tan, P., Liu, X. H., Liu, C. Y., Feng, J. Y., & Yang, K. (2024). Experimental study on heat transfer performance of a series combined microchannel heat dissipation system based on Al2O3 nanofluid. *Applied Thermal Engineering, 240*, 122237. https://doi.org/10.1016/j.applthermaleng.2023.122237

Vinoth, R., & Senthil Kumar, D. (2018). Experimental investigation on heat transfer characteristics of an oblique finned microchannel heat sink with different channel cross sections. *Heat Mass Transfer, 54*, 3809-3817. https://doi.org/10.1007/s00231-018-2398-z

Wu, T., Wang, L. Z., Tang, Y. C., Yin, C., & Li, X. K. (2022). Flow and heat transfer performances of liquid metal based microchannel heat sinks under high temperature conditions. *Micromachines, 13*(1), 95. https://doi.org/10.3390/mi13010095

Xia, Y., Chen, L., Luo, J. W., & W. Tao (2023). Numerical investigation of microchannel heat sinks with different inlets and outlets based on topology optimization. *Applied Energy, 330*, 120335. https://doi.org/10.1016/j.apenergy.2022.120335

Xiang, J. H., Deng, L. M., Zhou, C., Zhao, H. L., Huang, J. L. & S. L. Tao (2022). Heat transfer performance and structural optimization of a novel micro-channel heat sink. *Chinese Journal of Mechanical Engineering, 35*(1), 38. https://doi.org/10.1186/s10033-022-00704-5

Xu, F., & Wu, H. (2018). Experimental study of water flow and heat transfer in silicon micro-pin-fin heat sinks. *Journal of Heat Transfer, 140*(12), 122401. https://doi.org/10.1115/1.4040956

Fan, Y., Chen, C., Fu, R., Wang, Q., Cao, L., Chen, X., ... & Kang, J. (2024). Heat transfer performance study of fluid rotating microchannel heat sink, *Case Studies in Thermal Engineering, 58*, 104390, ISSN 2214-157X. https://doi.org/10.1016/j.csite.2024.104390

Yue, L., Qi, C., & Tang, M. (2024). A novel composite bionic leaf vein and honeycomb microchannel heat sink applied for thermal management of electronic components. *Appl. Therm. Eng., 252*, 123716. https://doi.org/10.1016/j.applthermaleng.2024.123716

Zeng, L., Deng, D. X., Zhong, N. B., & Zheng, G. S. (2021). Thermal and flow performance in microchannel heat sink with open-ring pin fins. *International Journal of Mechanical Sciences, 200*, 106445. https://doi.org/10.1016/j.ijmecsci.2021.106445

Zhao, C. Y., & Lu, T. J. (2002). Analysis of microchannel heat sinks for electronics cooling. *International Journal of Heat and Mass Transfer, 45(24)*, 4857-4869. https://doi.org/10.1016/S0017-9310(02)00180-1

Zhao, X. H., Su, L. M., Jiang, J., Deng, W. Y., & Zhao, D. (2023). A review of working fluids and flow state effects on thermal performance of micro-channel oscillating heat pipe for aerospace heat dissipation. *Aerospace, 10*(2), 179. https://doi.org/10.3390/aerospace10020179

Zheng, R., Wu, Y. J., Li, Y. H., Wang, G. L., Ding, G. F., & Sun Y. N. (2020). Development of a hierarchical microchannel heat sink with flow field reconstruction and low thermal resistance for high heat flux dissipation. *International Journal of Heat and Mass Transfer, 182*, 121925. https://doi.org/10.1016/j.ijheatmasstransfer.2021.121925